Kiyoshi Ueda *Editor*

Ultrafast Electronic and Structural Dynamics

Ultrafast Electronic and Structural Dynamics

Kiyoshi Ueda
Editor

Ultrafast Electronic and Structural Dynamics

Springer

Editor
Kiyoshi Ueda
Tohoku University
Sendai, Japan

If disposing of this product, please recycle the paper.

Preface

A natural time scale of the movement of electrons in matter, or the electronic wave packet motion, is of the order of tens to hundreds attoseconds (as). 1 as corresponds to 10^{-18} s. One atomic unit in time is ~24 as. This is the intrinsic smallest time under which an electron takes a circle on the first Bohr orbital divided by 2π. Thanks to the recent developments of laser technologies, catching electron motions in matter is no longer a dream but a tangible reality. The 2023 Nobel Prize in Physics was awarded jointly to Pierre Agostini, Ferenc Krausz, and Anne L'Huillier "for methods that generate attosecond pulses light for the study of electron dynamics in matter".

A natural time scale of the movement of atoms in matter is of the order of tens to hundreds of femtoseconds. 1 fs is 10^{-15} s. The fastest atomic motion is the vibration of the hydrogen molecule, and its vibrational period is ~8 fs. The 1999 Nobel Prize in Chemistry was awarded to Ahmed H. Zewail for "for showing that it is possible with rapid laser technique to see how atoms in a molecule move during a chemical reaction". This area, called femtochemistry, has been developed significantly in the last decades, thanks to the developments of X-ray free electron lasers (XFEL) and ultrafast electron diffractions (UED) that allow us to make a 3D molecular movie of atomic motions during chemical reactions and structural changes of matter.

On the other hand, time scales of the macroscopic structural changes, energy transfers, proton transfers, etc. in functional materials and macromolecules are significantly slower than the above-described time scales. These range from picoseconds (ps; 1 ps $= 10^{-12}$ s) to milliseconds (ms; 1 ms $= 10^{-3}$ s) because these slow processes are caused by a series of chain reactions. These slow dynamics are directly related to the functionalities of matter and living species. Here, again newly developed XFEL-based 3D molecular movie camera is opening a new route to investigate, e.g., protein's functionalities.

The present book describes time-resolved studies on atoms, molecules, condensed matters, and proteins in a wide range of time scales from attoseconds to milliseconds for the study of electronic and structural dynamics and the resulting functions of matters. We start with attosecond electron dynamics in atoms, molecules, liquids, and solids, then move to femtosecond structural dynamics in isolated molecules, molecules in solution, solids, and protein molecules, and finally picosecond to

millisecond structural dynamics, energy flow, proton tunneling and functions of proteins.

In Chap. 1, D. Busto, S. Zhong, J. M. Dahlström, A. L'Huillier, and M. Gisselbrecht describe how to study electron dynamics in atoms, focusing on the timescale for the photoelectric effect in atoms. In brief, they use high-order harmonic generation (HHG) in gases irradiated by an intense 800 nm near-infrared (NIR) laser pulse to create a train of extreme ultraviolet (XUV) attosecond pulses. The XUV photons ionize atoms in the presence of a *weak* fraction of the NIR pulses used for HHG, with a variable delay, and electrons are detected with an electron spectrometer. Two-photon transitions lead to the creation of sidebands in the photoelectron spectrum, which oscillate with the delay between the XUV and the NIR fields. From these RABBIT (reconstruction of attosecond beating by interference of two-photon transitions) measurements, attosecond time delays in atomic photoionization can be extracted. Theoretical backgrounds of photoionization time delays and the RABBIT technique are described in detail in this chapter.

The HHG spectrum by itself also includes the information about the electron dynamics in matter induced by an *intense* IR pulse, which is the origin of HHG in matter. In Chap. 2, M. Krüger and N. Dudovich describe how to make use of the HHG spectra to study such attosecond electron dynamics in atoms, molecules, and solids in intense fields. They use all-optical interferometry that allows them to access phase information and thus to reconstruct the electron wave packet dynamics. They discuss two approaches, internal and external interferometry. In internal interferometry, they manipulate the quantum paths within the HHG mechanisms and resolve the phase of the electron wave packet in strong IR laser-field processes. In the external interferometry, measuring amplitude and phase information of the harmonic light field through its interference with another light field, they determine the relative spectral phase of the two beams. We can see that both approaches reveal valuable information regarding the strong-field light-matter interaction as well as the atomic, molecular, or condensed system itself.

Water is essential to life. Attosecond dynamics in water may play an important role in chemical and biological processes that dominantly take place in water. In Chap. 3, H. J. Wörner, A. Schild, D. Jelovina, I. Jordan, C. Perry, T. Luu, and Z. Yin address attosecond dynamics in liquid water employing two experimental methods. The first one is attosecond photoelectron spectroscopy. This is closely related to the RABBIT method described in Chap. 1 but employs a liquid microjet as a target, which extends the applicability of RABBIT to most liquids and solutions. In addition, they employ "a principal-component analysis" of RABBIT data, which generalizes the extraction of photoionization delays to complex systems that often possess overlapping photoelectron spectra. They show that photoemission from liquid water is delayed by 50–70 as compared to photoemission from isolated water molecules at photon energies of 20–30 eV. The origin of the delays is fully discussed and experimentally supported by a RABBIT experiment on size-selected water clusters. The second method is HHG spectroscopy described in Chap. 2 but this first demonstration of

HHG in liquid opens a new route to study attosecond dynamics also in liquid, solutes, and solvents.

As can be seen in Chaps. 1–3, HHG represents a promising attosecond coherent light source in the XUV regime, playing a key role in attosecond science. As noted, HHG is a result of the interaction between an *intense* laser pulse and matter. Especially, attosecond electron dynamics driven by an ultrashort intense laser pulse in solids is of particular interest from the viewpoint of both fundamental physics and applications. In Chap. 4, K. L. Ishikawa, Y. Shinohara, T. Sato, and T. Otobe theoretically discuss momentum-space strong-field electron dynamics in graphene, crystalline dielectrics, and semiconductors, focusing on HHG and tunneling effect in solids.

On a fundamental level, the underlying mechanism behind almost any optical phenomenon is the light-driven motion of charges on atomic dimensions in space and time, as noted above. Visualizing such dynamics, however, requires ängstrom resolution in space and attosecond resolution in time. In Chap. 5, P. Baum and Y. Morimoto describe how to reach this goal using attosecond *electron* pulses in diffraction and microscopy, together with the first proof-of-concept experiments.

Chapters 1–5 discuss attosecond electron dynamics, or coherent electronic wave packet motion in the system, where the atomic motions in the systems are assumed to be frozen in these time scales. On the other hand, Chaps. 6–11 discuss femtosecond structural dynamics due to atomic motions that occur in tens to hundreds of femtoseconds in various systems. All the structural dynamics discussed here are photoinduced dynamics. In such photoexcited systems, coherent atomic motions, or nuclear wave packet dynamics such as vibrations in molecules and phonons in solids are induced. Along these atomic motions, various types of reactions, such as isomerization and intersystem crossing in molecules, light-induced phase transitions in solids, etc. take place. During these non-adiabatic reactions, electronic and nuclear degrees of freedom cannot be described independently. The main subject here would then be how to probe the coherent motion of atoms in matter that may vary through non-adiabatic reactions. It is worth noting that, even if the coherent electronic wave packet studied in Chaps. 1–5 is created upon photoexcitation, it may dephase quickly during the atomic motions. Thus, in most cases, the implicit assumption in Chaps. 6–11 is that the photoexcitation creates mainly coherent nuclear wave packet in a particular electronic state in the systems.

In Chap. 6, M. Yamazaki, T. Endo, A. Hishikawa, and M. Takahashi describe two experimental approaches that aim to visualize the change of molecular orbital pattern of isolated molecules during a light-induced intramolecular reaction. One is to employ electron momentum spectroscopy, which is known as a versatile tool to visualize the molecular orbital in a momentum space, to photoexcited molecules (S_2 acetone and S_1 toluene), in a time-resolved manner. Another attempt is to measure ultrafast laser tunneling ionization of photoexcited molecules. The tunneling ionization comes from the outermost molecular orbital and its rate is enhanced when the electron cloud is along the laser polarization direction. Here, they employ ion momentum imaging of fragment ions produced by dissociative ionization to image the outermost molecular orbital of photoexcited NO molecules. We can see both

approaches offer opportunities for investigating chemical reactions via time-resolved molecular orbital imaging.

As noted above, the advent of ultrafast pulsed XFELs with very high brightness has enabled the determination of transient molecular structures of molecules in excited states and undergoing chemical dynamics using X-ray scattering. Chapter 7 by P. M. Weber, B. Stankus, and A. Kirrander provides an introduction to X-ray scattering theory and considers several important aspects relating to the experimental implementation as well as the interpretation of the experiments. We can see here that ultrafast gas-phase X-ray scattering provides new observables to elucidate the dynamics of chemical reactions by providing complete, time-dependent molecular structures. Notably, the experiments also yield valuable information beyond molecular structure, such as the redistribution of electron density in excited states or the identification of the transition dipole moment in a molecule via the anisotropy of the scattering pattern.

In Chap. 8, J. Yang, M. Centurion, X. Wang, Th. Wolf, and M, Gühr show that also UED from isolated molecules allows insight into ultrafast quantum wave packet dynamics of molecules with sub-ångstrom spatial resolution. For the simple example of an excited state vibrational wave packet in iodine, they reconstruct the mean atomic distance as a function of delay after the optical excitation. For the case of CF_3I, they reconstruct the dissociative motion after UV excitation on the A-band states. They also show how the signature of non-adiabatic wave packet dynamics is visible in the diffraction data.

As seen in Chaps. 7 and 8, revealing details of coherent atomic motions during photochemical reactions on the femtosecond timescale is crucial for understanding the reaction mechanism in the photoexcited molecules. In Chap. 9, T. Katayama, T. J. Penfold, and Ch. Bressler describe how coherent atomic motions, or vibrational wave packets, are observed employing another experimental technique, i.e., time-resolved X-ray absorption near edge structure (TR XANES) spectroscopy with XFELs. TR XANES is sensitive not only to the local electronic structure changes but also to the structural dynamics in the vicinity of the selected absorbing atom. Since no long-range order information is required, it is highly suited to study disordered systems without any crystalline order, such as solvated transition metal complexes in the solution phase. Here, they present experimental studies on femtosecond vibrational modes for two prototypical transition metal complexes in solution.

In Chap. 10, M. Trigo, M. P. M. Dean, and D. A. Reis discuss structural and electronic dynamics in solids. The experimental techniques they introduce include XFEL-based time-resolved X-ray diffraction (TR XRD) and time-resolved resonant inelastic X-ray scattering (TR RIXS). As showcase examples, they first describe coherent phonon spectroscopy with TR XRD and its application to study couplings among coupled charge, spin, orbital, and lattice degrees of freedom in the photoexcited states, where the optical excitation is used to alter this delicate balance and produce properties not accessible in equilibrium. Then they show case studies in which the *intense* pump induces non-adiabatic dynamics exemplified by lattice symmetry changes. TR RIXS is also very powerful to study variations of charge, orbital, and spin degrees of freedom. Here, they describe the first TR RIXS measurement on a magnon.

Chapter 11 is the last chapter on femtosecond molecular dynamics and the first chapter on proteins. Here, A. Yabushita firstly describes details on ultrafast transient absorption spectroscopy setup developed for probing *primary* photochemical reactions of proteins. Ultrafast transient absorption signals of proteins also show modulation reflecting the real-time motion of the molecular vibration in time domain. Thus, time-gated Fourier analysis of the signal elucidates the temporal variation of the molecular vibration frequency, which elucidates molecular structural change during the primary photoreaction. Two showcase experiments are presented for ultrafast photoisomerization in bacteriorhodopsin (BR) and its mutants and ultrafast photo-dissociation in nitric oxide synthase.

As seen in Chaps. 7–11, the primary photoreactions start with coherent atomic motions in any form of matter, including proteins, but such vibrational coherences dephase in longer time scales, say, above 1 ps, as seen in these chapters. Chapters 12–15, on the other hand, focus on such long timescale reactions in the range of picoseconds to milliseconds in proteins, where coherent vibrational wave packet no longer plays a role because of dephasing. This long timescale is also very important because protein's functions appear in this time range because of chain reactions initiated by the primary reactions, such as the ones described in Chap. 11.

In Chap. 12, Y. Mizutani, S. Yamashita, and M. Mizuno describe time-resolved Raman mapping of protein energy flow that occurs in the time scale in tens of picoseconds. Their main interest is to provide a microscopic picture of energy dissipation on the atomic spatial scale. Heme proteins are ideal molecular systems to study energy flow because a photoexcited heme group is converted to an electronically ground state via ultrafast internal conversion and thus excess vibrational energy can be deposited locally at the heme site in proteins immediately after the photoexcitation. In consequence, heme acts as a very efficient energy convertor. To observe subsequent energy relaxation processes, they adopted anti-Stokes ultraviolet resonance Raman (UVRR) spectroscopy. Because of the resonance effect, UVRR spectroscopy probes Raman bands of aromatic amino acid residues with high selectivity, allowing site-selective detection of energy at the level of a single amino acid residue in a large protein molecule.

In Chap. 13, D. Zigmantas and T. Mančal introduce another powerful experimental method to study energy transfer and couplings within molecular assemblies, i.e., two-dimensional electronic spectroscopy (2DES). They review firstly the theoretical foundation for understanding of 2DES signals in molecular systems and then discuss encompassing crucial aspects of experimental implementations of 2DES. Illustrative applications of 2DES to investigate light-harvesting functions in an isolated pigment-protein complex and an intact photosynthetic unit in green sulfur bacteria reveal the extensive insights into the photophysical functions of photosynthetic machinery. The time range of revealed energy transfer processes is in the range from 50 fs to 250 ps.

In Chap. 14, A. Benabbas and P. M. Champion discuss the use of vibrational coherence and ultrafast wide dynamic-range population kinetics to probe biological molecules. They use impulsive stimulated Raman scattering to develop the method of vibrational coherence spectroscopy, which reveals both the structural and functional aspects of the difficult to detect low-frequency modes in proteins. Studies of electron

tunneling in cytochrome c as well as the kinetics of the methionine–heme binding reaction are emphasized. They also examine vibrational coherence and its potential participation in the excited state proton transfer of green fluorescent proteins and conclude that coherent motion does not affect the excited state proton transfer rate that occurs on the ps timescale. For the ground-state proton back-transfer reaction, they find that (incoherent) vibrationally assisted proton tunneling is the dominant transport channel and that the tunneling rate is ~400 ps at room temperature.

The last Chap. 15 by A. M. Orville, E. Nango, S. Iwata, S. Mous, J. Standfuss, P. Nogly, M. Suga, J.-R. Shen, and M. Kubo is dedicated to time-resolved serial femtosecond X-ray crystallography (SFX) of protein molecules. XFELs offer new opportunities in structural biology, especially for samples at near-physiological conditions and for time-resolved studies that link together the analysis of structure and function within the same samples, with the crystal size requirements such that even submicron crystals can yield high-quality diffraction data. SFX is a new technique developed to exploit the fs pulses from XFELs and to use thousands of micronsize crystals or smaller. This chapter starts with an introduction to SFX by Orville. Then, Nango, Iwata, Mous, Standfuss, and Nogly describe the structure, function, and dynamics of the light-driven proton pump, bacteriorhodopsin. The time range covered here is from tens of femtoseconds (primary isomerization) to milliseconds (functions). Next, Suga and Shen summarize results from photosystem II, one of the hottest topics in time-resolved SFX. Kubo concludes the chapter with an example of a caged nitric oxide compound driving the P450nor enzyme reaction, which is an unusual member of the P450 superfamily of heme-dependent proteins.

I thank all the above-listed chapter authors for their invaluable contributions to this book.

Sendai, Japan   Kiyoshi Ueda

Contents

Contributors

Peter Baum Universität Konstanz, Konstanz, Germany

Abdelkrim Benabbas Department of Physics and Center for Interdisciplinary Research on Complex Systems, Northeastern University, Boston, MA, USA

Christian Bressler European XFEL, Schenefeld, Germany;
The Hamburg Centre of Ultrafast Imaging, Hamburg, Germany;
Department of Physics, Universität Hamburg, Hamburg, Germany

David Busto Department of Physics, Lund University, Lund, Sweden

Martin Centurion Department of Physics and Astronomy, University of NE–Lincoln, Lincoln, NE, USA

Paul M. Champion Department of Physics and Center for Interdisciplinary Research on Complex Systems, Northeastern University, Boston, MA, USA

Jan Marcus Dahlström Department of Physics, Lund University, Lund, Sweden

Mark P. M. Dean Condensed Matter Physics and Materials Science Department, Brookhaven National Laboratory, Upton, NY, USA

Nirit Dudovich Weizmann Institute of Science, Department of Physics of Complex Systems, Rehovot, Israel

Tomoyuki Endo Kansai Institute for Photon Science, National Institutes for Quantum Science and Technology, Kyoto, Japan

Mathieu Gisselbrecht Department of Physics, Lund University, Lund, Sweden

Markus Gühr Deutsches Elektronen-Synchrotron DESY, Hamburg, Germany

Akiyoshi Hishikawa Department of Chemistry, Graduate School of Science, Nagoya University, Nagoya, Japan;
Research Center for Materials Science, Nagoya University, Nagoya, Japan

Kenichi L. Ishikawa Department of Nuclear Engineering and Management, Graduate School of Engineering, The University of Tokyo, Bunkyo-ku, Tokyo, Japan

So Iwata RIKEN SPring-8 Center, Hyogo, Japan;
Department of Cell Biology, Graduate School of Medicine, Kyoto University, Kyoto, Japan

Denis Jelovina Laboratorium für Physikalische Chemie, ETH Zürich, Zürich, Switzerland

Inga Jordan Laboratorium für Physikalische Chemie, ETH Zürich, Zürich, Switzerland

Tetsuo Katayama Japan Synchrotron Radiation Research Institute, Sayo, Hyogo, Japan;
RIKEN, Sayo, Hyogo, Japan

Adam Kirrander Department of Chemistry, Physical and Theoretical Chemistry Laboratory, University of Oxford, Oxford, UK

Michael Krüger Technion – Israel Institute of Technology, Department of Physics and Solid State Institute and Helen Diller Quantum Center, Haifa, Israel

Minoru Kubo Graduate School of Science, University of Hyogo, Ako, Hyogo, Japan

Anne L'Huillier Department of Physics, Lund University, Lund, Sweden

Tran Trung Luu Laboratorium für Physikalische Chemie, ETH Zürich, Zürich, Switzerland

Tomáš Mančal Faculty of Mathematics and Physics, Charles University, Prague, Czech Republic

Misao Mizuno Department of Chemistry, Graduate School of Science, Osaka University, Toyonaka, Osaka, Japan

Yasuhisa Mizutani Department of Chemistry, Graduate School of Science, Osaka University, Toyonaka, Osaka, Japan

Yuya Morimoto RIKEN Cluster for Pioneering Research and RIKEN Center for Advanced Photonics, RIKEN, Wako, Saitama, Japan

Sandra Mous Linac Coherent Light Source, SLAC National Accelerator Laboratory, Menlo Park, USA

Eriko Nango RIKEN SPring-8 Center, Hyogo, Japan;
Institute of Multidisciplinary Research for Advanced Materials, Tohoku University, Sendai, Miyagi, Japan

Przemyslaw Nogly Dioscuri Centre for Structural Dynamics of Receptors, Faculty of Biochemistry, Biophysics and Biotechnology, Jagiellonian University, Kraków, Poland

Allen M. Orville DiamondLight Source Ltd., Didcot, UK; Harwell Science and Innovation Campus, Didcot, UK

Tomohito Otobe Ultrafast Dynamics Group, National Institutes for Quantum and Radialogical Science and Technology (QST), Kizugawa, Kyoto, Japan

Thomas J. Penfold Chemistry-School of National and Environmental Sciences, Newcastle University, Newcastle Upon-Tyne, UK

Conaill Perry Laboratorium für Physikalische Chemie, ETH Zürich, Zürich, Switzerland

David A. Reis Stanford PULSE Institute and Stanford Institute for Materials and Energy Sciences (SIMES), SLAC National Accelerator Laboratory, Menlo Park, CA, USA

Takeshi Sato Department of Nuclear Engineering and Management, Graduate School of Engineering, The University of Tokyo, Bunkyo-ku, Tokyo, Japan

Axel Schild Laboratorium für Physikalische Chemie, ETH Zürich, Zürich, Switzerland

Jian-Ren Shen Graduate School of Environmental, Life, Natural Science and Technology, Research Institute for Interdisciplinary Science, Okayama University, Okayama, Japan

Yasushi Shinohara Photon Science Center, Graduate School of Engineering, The University of Tokyo, Bunkyo-ku, Tokyo, Japan

Joerg Standfuss Laboratory of Biomolecular Research, Biology and Chemistry Division, Paul Scherrer Institute, Villigen PSI, Switzerland

Brian Stankus Department of Chemistry, Western Connecticut State University, Danbury, Connecticut, USA

Michihiro Suga Graduate School of Environmental, Life, Natural Science and Technology, Research Institute for Interdisciplinary Science, Okayama University, Okayama, Japan

Masahiko Takahashi Institute of Multidisciplinary Research for Advanced Materials, Tohoku University, Sendai, Japan

Mariano Trigo Stanford PULSE Institute and Stanford Institute for Materials and Energy Sciences (SIMES), SLAC National Accelerator Laboratory, Menlo Park, CA, USA

Xijie Wang Fakultät für Physik, Universität Duisburg Essen, Essen, Germany

Peter M. Weber Department of Chemistry, Brown University, Providence, Rhode Island, USA

Thomas Wolf SLAC National Accelerator Laboraty, Menlo Park, USA

Hans Jakob Wörner Laboratorium für Physikalische Chemie, ETH Zürich, Zürich, Switzerland

Atsushi Yabushita Department of Electrophysics, National Yang Ming Chiao Tung University, Hsinchu, Taiwan;
Research Institute for Engineering, Kanagawa University, Yokohama, Japan

Satoshi Yamashita Department of Chemistry, Graduate School of Science, Osaka University, Toyonaka, Osaka, Japan

Masakazu Yamazaki Department of Chemistry, School of Science, Tokyo Institute of Technology, Tokyo, Japan

Jie Yang Center of Basic Molecular Science, Department of Chemistry, Tsinghua University, Beijing, China

Zhong Yin Laboratorium für Physikalische Chemie, ETH Zürich, Zürich, Switzerland

Shiyang Zhong Department of Physics, Lund University, Lund, Sweden

Donatas Zigmantas Chemical Physics, Lund University, Lund, Sweden

Chapter 1
Attosecond Dynamics of Non-resonant Atomic Photoionization

David Busto, Shiyang Zhong, Jan Marcus Dahlström, Anne L'Huillier, and Mathieu Gisselbrecht

Abstract The interaction of light with matter played a key role in the establishment of quantum mechanics, and each development of new light sources led to important advances in science, technology and society. An exciting area of physics has been opened with the new millennium, attosecond physics, where the motion of electrons can be studied at the fastest time scale ever reached with light. We review the field of non-resonant photoionization of rare gases using attosecond pulses, with an emphasis on the theoretical background of the reconstruction of attosecond beating by interference of two-photon transition (RABBIT) measurement technique. This approach allows the description of photoionization in the time domain while keeping a high spectral resolution. Examples show the status and the progress in the field during the last decade.

1.1 Introduction

The interaction of electromagnetic radiation with matter has considerably contributed to our understanding of the quantum nature of the microcosmos. Photoionization is one of the most fundamental processes in nature, that occurs when a high-energy photon is absorbed. Since its explanation by Einstein [1], which supported the concept of light quanta, a comprehensive quantum mechanical description of atomic photoionization has been achieved, thanks to the advent of synchrotron radiation light sources in the 1960s and the progress in photoelectron detection techniques [2]. An important aspect of photoionization studies is to characterize the partial amplitudes and the relative phases between the ionization channels. One of the goals is to perform

---

The original version of the chapter has been revised: The incorrect name has been updated. A correction to this chapter can be found at https://doi.org/10.1007/978-981-97-2914-2_16

D. Busto · S. Zhong · J. M. Dahlström · A. L'Huillier · M. Gisselbrecht (✉)
Department of Physics, Lund University, Box 118, 221 00 Lund, Sweden
e-mail: mathieu.gisselbrecht@sljus.lu.se

A. L'Huillier
e-mail: Anne.Lhuillier@fysik.lth.se

'complete' experiments in order to capture the dynamics between different photoionization channels [3–5]. Experimentally, specific requirements have to be met [2]. The energy resolution should be high enough to disentangle the ionization channels leading to different ionic states. Angular resolution is needed to quantify the interference between paths leading to the same final ionic state, which results in anisotropic angular distributions [6, 7]. Finally, in most atomic systems, the magnetic sub-levels of the initial state are degenerate in energy. Without the detection of the outgoing electron spin [8–10] and the alignment and/or orientation of the residual ion [11], the relative contribution of these channels cannot be deduced from the measurement. The combination of laser and synchrotron radiation has led to new ways to perform 'complete' experiments [12]. In particular, resonant two-photon ionization schemes allow the manipulation of the alignment of the atoms with the light polarization, thus recovering the relative phase of different ionization channels. Hence, in-depth studies of photoemission with ever-increasing energy and angle resolution, have been performed to benchmark theoretical treatments in a variety of excited atoms [13].

The generation of high-order harmonics of a laser in a gas is one of the most recognized non-linear processes that lead to the emission of coherent radiation in the eXtreme UltraViolet (XUV) range. Discovered in the late 80's [14, 15], the unique properties of this radiation opened new ionization schemes, such as two-colour non-resonant photoionization from the ground state of rare gases [16–18], combining harmonics and infrared (IR) laser radiation. In parallel to the exploration of applications of this new radiation, world-wide efforts were devoted to understand, optimize and control the high-order harmonic generation (HHG) process [19, 20]. The exploitation of the attosecond (1 as = 10^{-18}s) temporal structure of this XUV radiation began at the beginning of the millennium, following a series of seminal experiments [21, 22]. Since the energy spectrum of attosecond light sources lies essentially above the ionization threshold of atoms, photoionization is central to many applications.

An electron emitted after the absorption of an attosecond pulse is no longer well-defined in momentum space but is characterized by a momentum distribution, i.e. an Electron Wave-Packet (EWP). Its dispersion directly provides information on both the temporal properties of the light pulse and the potential seen by the escaping electron from the target. In particular, when applied to photoionization, the concept of scattering delays, introduced by Eisenbud, Wigner and Smith [23–25] in the 1950s–1960s, implies that when the electron propagates in the ionic potential, it acquires a delay relative to a reference wave-packet propagating in vacuum.

This information is extracted with the help of experimental techniques, such as streaking [26] and RABBIT[1] [22]. Using these techniques, photoionization time delays were measured for the first time at the beginning of the 2010's [27, 28]. The theoretical foundations for extracting dynamical information on photoionization from streaking or RABBIT experiments have been thoroughly discussed and reviewed, e.g. in [29–31]. Numerous experimental studies have been performed in different atomic systems and spectral regions, e.g. close to threshold [32–35],

---

[1] Various spellings of the acronym can be found in the literature. The present convention is based on the practices of the optical community.

autoionizing resonances [36–42] or Cooper minima [28, 43–45], over broad ranges [27, 46–48], including satellite transitions [49], double ionization [50] and/or Auger decay [51, 52]. Finally, in the recent years, a strong effort has been devoted to characterize the dynamics between different photoionization channels [53–56], with the aim of performing 'complete' experiments.

The development of the next generation of attosecond light sources [57] with higher flux [58, 59], repetition rate [60–62], exotic polarization state [63–66] and photon energies extending in the soft X-ray regime [67, 68] motivates the present review of attosecond atomic photoionization. We present in Sect. 1.2 the quantum mechanical description of photoionization by absorption of one and two photons. In Sect. 1.3, we discuss how the interferometric RABBIT technique, based on two-photon ionization, can be applied to determine the photoionization phase and amplitude in angle-integrated and angular-resolved experiments. Finally, in Sect. 1.4 we provide experimental details and examples showing how photoionization can be characterized in the temporal domain while keeping high spectral resolution.

1.2 Theoretical Background

The photoionization process provides a unique ground for fundamental studies of many-body effects and in particular electron-electron interactions. Its quantum mechanical description requires the knowledge of the atomic ground state wave function, which can be computed rather straightforwardly in centro-symmetric systems, and the final state wave function, which is the most demanding for theoretical formulation and numerical treatment. Indeed, the continuum wave function is generally expanded, using scattering theory, in partial waves, where a complete set of quantum numbers characterize both the electron and the residual ionic core. In the most general case, this fragmentation of the initial system into an ion core and photoelectron is subject, among other things, to angular momentum couplings and electron–electron interactions. Here, we will discuss, for the sake of simplicity, the case of one-photon and two-photon single ionization within the central field approximation for a single active electron.

1.2.1 Photoionization with Attosecond Pulses

Atoms exposed to XUV attosecond pulses get ionized. The photoionization transition amplitude can be calculated within first-order perturbation theory, due to the weak intensity of the electromagnetic field of the attosecond pulses, and can be written as

$$\mathcal{A}_{fg} = -\frac{i}{\hbar} \int dt \left\langle \varphi_f \right| T(t) \left| \varphi_g \right\rangle e^{i\Omega_{fg}t}, \tag{1.1}$$

where $\hbar$ is the reduced Planck constant, $|\varphi_f\rangle$ and $|\varphi_g\rangle$ represent the final continuum state and the ground state with respective energies ε_f and ε_g and $\Omega_{fg} = (\varepsilon_f - \varepsilon_g)/\hbar$ is the Bohr angular frequency. The atom–photon interaction operator, $T(t)$, is an expansion of electric and magnetic multipoles [69], which can be reduced to the non-relativistic dipole term in the spectral region spanning from 1 nm to 100 nm.[2]

Since attosecond pulses are in most cases linearly polarized [71], we consider in the following the electrical field of the attosecond pulses, $\tilde{\mathcal{E}}_{\mathrm{XUV}}(t)$, to be along the $\hat{z}$ axis. Within the dipole approximation, the interaction of the light field with an atom can be expressed in the length gauge form as

$$T(t) = e\tilde{\mathcal{E}}_{\mathrm{XUV}}(t)z. \tag{1.2}$$

1.2.1.1 Electron Wave-Packet in the Continuum

Using scattering states $\varphi_{\mathbf{k}}$, where $\mathbf{k}$ is the electron wave vector as final continuum states and Eq. (1.2), Eq. (1.1) become

$$\mathcal{A}_{\mathbf{k}g} = -\frac{ie}{\hbar} \int dt \tilde{\mathcal{E}}_{\mathrm{XUV}}(t) e^{i\Omega_{\mathbf{k}g}t} \langle \varphi_{\mathbf{k}}| z |\varphi_g\rangle, \tag{1.3}$$

which, using $\mathcal{E}_{\mathrm{XUV}}$, equal to the Fourier transform of the attosecond pulse electric field, $\tilde{\mathcal{E}}_{\mathrm{XUV}}$, takes the simple form,

$$\mathcal{A}_{\mathbf{k}g} = -\frac{ie}{\hbar} \mathcal{E}_{\mathrm{XUV}}(\Omega_{kg}) \langle \varphi_{\mathbf{k}}| z |\varphi_g\rangle. \tag{1.4}$$

Attosecond pulses have a large bandwidth of typically a few tens of eV. $\mathcal{A}_{\mathbf{k}g}$ is a distribution in momentum space, which represents the electron wave-packet created by absorption of the XUV attosecond pulses.

The scattering states $\varphi_{\mathbf{k}}$ (normalized in momentum) can be expanded in partial waves as [72]

$$\varphi_{\mathbf{k}}(\mathbf{r}) = \frac{1}{\sqrt{k}} \sum_{L=0}^{\infty} \sum_{M=-L}^{M=L} i^L e^{-i\eta_L(k)} Y_{LM}^*(\hat{k}) R_{kL}(r) Y_{LM}(\hat{r}). \tag{1.5}$$

where L and M are the electron orbital angular momentum and magnetic quantum number, respectively, $\hat{r} = \mathbf{r}/r$ and $\hat{k} = \mathbf{k}/k$. The R_{kL} radial wave functions are normalized as $\langle R_{kL}|R_{k'L}\rangle = \delta(\varepsilon_k - \varepsilon_{k'})$, and Y_{LM} are spherical harmonics. The scattering phase $\eta_L(k)$ can be decomposed into two contributions $\eta_L = \sigma_L + \delta_L$, where σ_L is the universal Coulomb phase shift due to the singularity at the origin and δ_L is an atom-specific phase shift originating from modifications of the short-range potential due to electron correlations. The asymptotic radial wave function of the fully

---

[2] See [70] for a report on the contribution of higher order terms in the soft X-ray region.

fragmented atom (ion with a free electron) is a modified plane wave [29, 73],

$$\lim_{r \to \infty} R_{kL}(r) = \sqrt{\frac{2}{\pi k}} \frac{1}{r} \sin \left[kr + \frac{Z \ln(2kr)}{k} + \eta_L(k) - \pi L/2 \right], \qquad (1.6)$$

where Z is the charge of the ion. This expression shows that an electron propagating away from the ion core accumulates a phase shift. This phase shift, $\phi_{kL}(r)$, includes the effect of the long-range Coulomb potential through a r-dependent phase, $Z \ln(2kr)/k$, the contribution of the short-range potential, $\eta_L(k)$ and a centrifugal term, $-\pi L/2$, that depends on the scattering channel. Consequently, for an EWP that contains a distribution of wave vectors $\mathbf{k}$, different accumulated phases will contribute to the EWP dispersion. This EWP dispersion will thus differ from a free EWP and will entail information on the photoionization energy dependence and short-range electron correlations.

1.2.1.2 Photoionization Time Delays

The concept of time delay was first introduced more than 60 years ago by Eisenbud, Wigner and Smith [23–25] in the framework of scattering theory for a short-range potential, $V(r)$. As the EWP propagates in the potential, the local momentum of the electron, given by

$$\hbar k(r) = \sqrt{2m_e[E - V(r)]}, \qquad (1.7)$$

where E is the electron kinetic energy, varies. This local variation of momentum, and hence of the EWP phase, leads to a global phase shift $\phi = 2\eta$ compared to an EWP propagating in free space. Consequently, the outgoing wave-packet acquires an effective group delay τ_S defined similarly to that of an optical wave-packet,

$$\tau_S = \hbar \frac{\partial \phi}{\partial E} = 2\hbar \frac{\partial \eta}{\partial E}. \qquad (1.8)$$

Photoionization is a half-scattering process since the EWP only propagates through half of the potential ($r > 0$). As a result, using Eq. (1.6), the delay of the wave-packet relative to a free electron for the scattering channel characterized by the angular momentum L is given by[3]

$$
\begin{aligned}
\tau_{\text{EWP}} &= \hbar \frac{\partial}{\partial E} \left(\frac{Z \ln(2kr)}{k} + \eta_L(k) - \pi L/2 \right) \\
&= \hbar \frac{\partial}{\partial E} \left(\frac{Z \ln(2kr)}{k} \right) + \hbar \frac{\partial \eta_L}{\partial E} \\
&= \tau_{\text{Coul}}(k, r) + \tau_W(k, L),
\end{aligned}
\qquad (1.9)
$$

---

[3] Note that the difference of factor 2 compared to Eq. (1.8).

where $\tau_W(k, L)$ is called the Wigner time delay and is a finite quantity which can be interpreted in the same way as the time delay introduced by Wigner for a short range potential [Eq. (1.8)]. The term $\tau_{\text{Coul}}(k, r)$ is a universal position-dependent delay which accounts for the outgoing electron progressively slowing down because of the attractive Coulomb potential [30]. Because the range of the Coulomb interaction is infinite, it is not meaningful to compare the delay of the outgoing EWP to a free EWP, since it is not possible to define a radius after which the phase shift has converged to a stationary value. Instead, one can compare the delay between two EWPs originating from two different photoionization processes such that the contributions of $\tau_{\text{Coul}}(k, r)$ cancel out, and thereby study the difference between the Wigner time delays $\tau_W(k, L)$, which, as pointed out previously, influences the dispersion of the EWP.[4]

1.2.2 Laser-Assisted Photoionization

EWP group delays can be measured experimentally with techniques [22, 26] resembling those used in ultra-fast optics, such as cross-correlation and spectral interferometry. These techniques require, in addition to the XUV pulses, a probe laser field at a variable delay. We will consider here the weak-field regime, with only one- or two-photon transitions. This allows for a treatment of ionization within the framework of perturbation theory, up to second order.

1.2.2.1 Two-Photon Ionization

Without losing any generality, we use a monochromatic description of the XUV field [29]; for effects related to the finite pulse duration, see [75]. In a two-photon transition, an XUV photon with angular frequency Ω is absorbed, taking an electron from the ground state $\left|\varphi_g\right\rangle$ to an intermediate continuum state $|\varphi_v\rangle$, followed by further absorption or emission of a laser photon with angular frequency ω taking the electron to a final continuum state $|\varphi_{\mathbf{k}}\rangle$.[5] If both XUV and laser fields are linearly polarized along the z axis, the two-photon transition matrix element can be expressed as

$$M_{\mathbf{k}g}^{(\pm)}(\Omega) = -\frac{ie^2}{\hbar} \lim_{\epsilon \to 0^+} \sum_{\varphi_v} \frac{\langle\varphi_{\mathbf{k}}|z|\varphi_v\rangle \langle\varphi_v|z|\varphi_g\rangle}{\hbar\Omega - \varepsilon_v + \varepsilon_g + i\epsilon}. \tag{1.10}$$

The $(\pm)$ superscript in the matrix element indicates whether the laser photon is absorbed $(+)$ or emitted $(-)$ in the second step. The sum integral in Eq. (1.10) runs

---

[4] See [74] for a discussion of the concept of time in quantum mechanics.

[5] It is in principle possible that the laser interacts first, taking the electron to a virtual intermediate state. However, this process is in general very improbable and we do not consider it in the following.
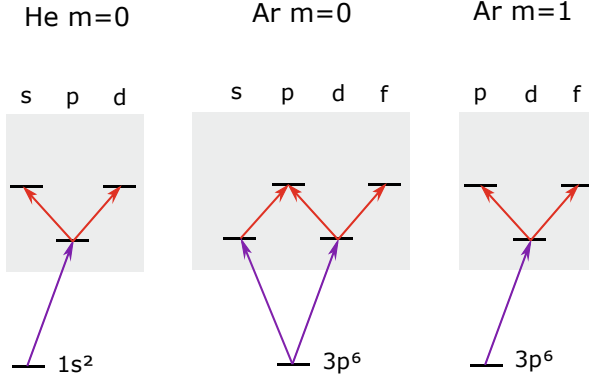
Fig. 1.1 Example of channel-resolved two-photon transitions in He and Ar when a laser photon is absorbed. Figure taken from [77]

over both continuum and discrete states, meaning that an infinite number of quantum paths can lead to the same final state $|\varphi_{\mathbf{k}}\rangle$. The intermediate state $|\varphi_\nu\rangle$ that conserves energy, $\varepsilon_\nu = \varepsilon_g + \hbar\Omega$, contributes most significantly to the transition, while the non-resonant states are required for a correct description of the phase of the two-photon transition [29]. The use of different polarizations between the XUV and the laser fields is discussed in [76].

Expanding in partial waves the final state [see Eq. (1.5)], one can express $M_{\mathbf{k}g}^{(\pm)}$ as a sum of angular-momentum paths that build up the total two-photon transition matrix element:

$$M_{\mathbf{k}g}^{(\pm)} = \sum_{L,\lambda} M_{L\lambda m}^{(\pm)} Y_{Lm}(\theta, \phi). \tag{1.11}$$

where $\hat{k}$ is represented in spherical coordinates by the angles of emission (θ, ϕ) and where the index m describes the magnetic number of the initial state, φ_g[6,7], while $L = \lambda \pm 1 \geq 0$, $\lambda = \ell_0 \pm 1 \geq 0$ and ℓ_0 are the orbital quantum numbers of the final, intermediate and initial states, respectively. Figure 1.1 shows examples of these angular-momentum paths in helium and argon, using the spectroscopic notation s, p, d and f to denote the orbital angular momentum.

Two-photon transitions involve Continuum–Continuum (CC) transitions between the intermediate and final states due to the laser field. Below, we examine the behaviour of the CC transitions in the absence of intermediate or final-state interactions.

---

[6] It is conserved in the two-photon process since both XUV and probe fields are linearly polarized in the same direction.

[7] If there are several initial states, e.g. with different m, the contributions of the EWPs created from the different initial states will add incoherently.
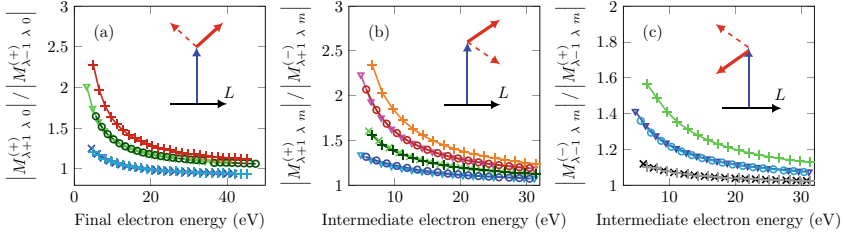
Fig. 1.2 Propensity rules in laser-assisted photoionization in He $1s$ ($\times$), Ne $2p$ (∇), Ar $3p$ ($\bigcirc$) and Kr $3d$ ($+$). The colour of the curves indicates the angular momentum of the intermediate state in **a** and final state in **b**, **c** [shades of grey s, shades of blue p, shades of green d, shades of red f and orange g]. **a** Probability ratio between increasing ($L = \lambda + 1$) and decreasing angular momentum ($L = \lambda - 1$) in the case of absorption of a photon from the intermediate state. **b** Probability ratio between absorbing and emitting a photon in the case of increasing angular momentum. **c** Probability ratio between emitting and absorbing a photon in the case of decreasing angular momentum. The insets present an energy and angular momentum diagram illustrating the propensity rule in each case. Figure taken from ref [34]. Licensed under CC-BY-4.0

1.2.2.2 Continuum–Continuum Transition Amplitudes—Fano's Propensity Rule

In 1985, Ugo Fano showed that for one-photon transitions, from the ground state to the continuum, the channel in which the angular momentum increases dominates over the channel in which angular momentum decreases [78]. For example, in neon, the transition $|2p\rangle \rightarrow |\epsilon d\rangle$ dominates over the transition $|2p\rangle \rightarrow |\epsilon s\rangle$. The validity of this propensity rule was investigated theoretically for CC transitions [34]. Figure 1.2(a–c) shows a comparison of the moduli of the different matrix elements in He, Ne, Ar outer shells and Kr $3d$ inner shell. In contrast to analytical expressions based on the Wentzel–Kramers–Brillouin (WKB) theory [29], and recently reformulated using hypergeometric functions [79], we here extract the CC transitions from two-photon transition matrix elements calculated using the Relativistic Random Phase Approximation (RRPA) for the first XUV photon absorption and an effective spherical potential for the second photon transition [80].

Figure 1.2a compares the probability of increasing or decreasing angular momentum when a photon is absorbed between two continuum states. In most cases, we find that the ratio $|M^{(+)}_{(\lambda+1)\lambda m}|/|M^{(+)}_{(\lambda-1)\lambda m}|$ is larger than one in agreement with Fano's propensity rule, which states that increasing orbital angular momentum is a more probable process.[8] Figure 1.2b, c compares the probability of absorbing or emitting a photon when angular momentum increases (b) or decreases (c). An increase of the orbital angular momentum ($L = \lambda + 1$) is more likely when a photon is absorbed while a decrease of the orbital angular momentum ($L = \lambda - 1$) is favoured when a photon is emitted. This result supports the idea that absorption and emission have time-reversal symmetry. Finally, it is worth noting that the ratios are independent of

---

[8] At high kinetic energy and low angular momentum, however, Fano's propensity rule is violated, as explained below.

the atomic species, i.e. the curves in Fig. 1.2 are universal and only depend on the intermediate angular momentum and electron kinetic energy.

The physical origin of this propensity rule can be discussed in terms of the local momentum of the electron in the continuum [see Eq. (1.7)]. The potential experienced by the electron has two contributions, $V_0(r)$, an atom-specific potential and $V_\ell(r)$ the centrifugal potential equal to

$$V_\ell(r) = \frac{\hbar^2 \ell(\ell+1)}{2m_e r^2}. \tag{1.12}$$

The strength of the transition between the intermediate and final states is highest when the difference in local momentum is the smallest. As a result, when the laser photon is absorbed, resulting in a higher kinetic energy E, increasing angular momentum is favoured as it increases the centrifugal potential. In the case where the laser photon is emitted, the total energy decreases thus favouring the transition to a lower angular momentum state.

Finally, when $E \gg \hbar\omega$, the matrix elements for laser-assisted absorption and emission processes become equal. In this limit, known as the soft-photon limit, the ratio of the two-photon matrix elements approaches asymptotic values that are given by ratios of the corresponding angular integrals of the dipole transitions in the continuum [81]. Due to the fact that angular integrals favour low angular momentum, a violation of Fano's propensity rule is observed at high energy for the $p \to d/s$ probability ratio, as seen in Fig. 1.2(a), blue curve, which tends to 0.8.

1.2.2.3 Continuum–Continuum Transition Phases

The phase of the two-photon transition matrix element is given by

$$\arg\left(M_{L\lambda m}^{(\pm)}\right) = \pi - \frac{\pi\lambda}{2} + \eta_\lambda(\kappa^{(\pm)}) + \phi_{CC}^{\lambda \to L}(k, \kappa^{(\pm)}), \tag{1.13}$$

where $\kappa^\pm$, k, with $\kappa^{(+)} < k < \kappa^{(-)}$, are the wave numbers of the electron in the intermediate and final states respectively, $\eta_\lambda(\kappa^{(\pm)}) = \eta_\lambda^{(\pm)}$ is the scattering phase in the intermediate state and $\phi_{CC}^{\lambda \to L}(k, \kappa^{(\pm)}) = \phi_{CC}^{(\pm)}(\lambda \to L)$ is the phase induced by the laser-driven continuum transition from $\kappa^{(\pm)}$ to k in the long-range Coulomb tail, for absorption $(+)$ and emission of a laser photon $(-)$. In the asymptotic approximation, valid at kinetic energy above 25–30 eV, the CC phase only depends on the final and intermediate wave numbers $\phi_{CC}^{(\pm)}(\lambda \to L) \sim \phi_{CC}^{(\pm)}$ [29]. This approximation has proved a useful tool for understanding the delays measured in various attosecond experiments [28, 43, 82].

Fano's propensity rule for CC transitions shows that, far from resonances, the amplitude of the transitions induced by interaction with the IR depends only on the angular momentum and kinetic energy of the electron. It is independent of the atom. Figure 1.3 shows that the same is true for the phase of the CC transitions. In
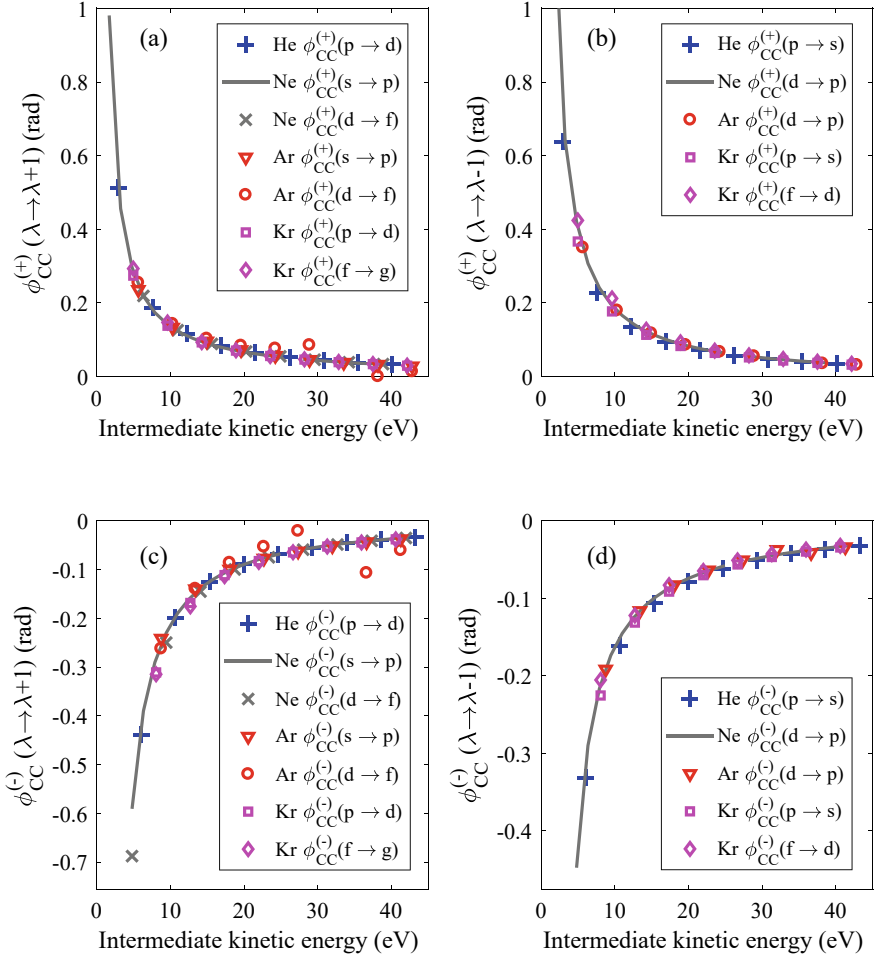
Fig. 1.3 Angular momentum dependence of the CC phases in He $1s$, Ne $2p$, Ar $3p$ and Kr $3d$. **a** CC phases for absorption of an IR photon and increase of angular momentum. **b** CC phases for absorption of an IR photon and decrease of angular momentum. **c** CC phases for emission of an IR photon and increase of angular momentum. **d** CC phases for emission of an IR photon and decrease of angular momentum

fact, contrary to the amplitude of the CC transitions, the phase of these transitions does not depend on the absolute value of the electron angular momentum, but only on whether the angular momentum increases or decreases in the transition. For example, Fig. 1.3(a) shows that $\phi^{(+)}(\lambda \rightarrow L)$ is almost identical for He (p→d), Ne (s→p), Ar (d→f) and Kr (f→g) over a large range of kinetic energies, as low as 5 eV. The same is true in the case of emission of an IR photon or in the case of channels with decreasing angular momentum, see Figs. 1.3(b–d). At low kinetic energy, both in the case of
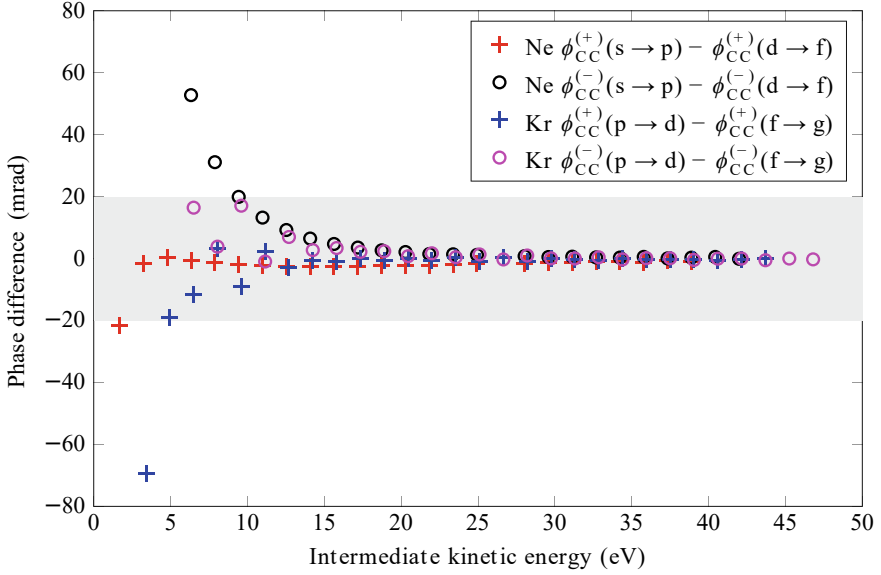
Fig. 1.4 Deviation from the universality of the CC phase in neon and krypton. For each atom, the phase difference between two CC transitions increasing angular momentum is shown. The shaded grey area corresponds to the region for which the phase difference is smaller than 20 mrad

absorption and emission, small differences between channels with increasing and decreasing angular momentum can be observed. We note, however, that contrary to the amplitude, the CC phase is more sensitive to strong spectral features such as Cooper minima. Fig. 1.3(c) shows that in argon, a deviation from the universal behaviour can be observed in the vicinity of the 3p Cooper minimum around 30 eV, while the propensity rule for transition amplitudes is not affected [83]. Additionally, at low kinetic energy, small difference between the different channels can also be observed.

Figure 1.4 presents the phase difference between different CC transitions increasing angular momentum in neon and krypton atoms. The figure shows that at high kinetic energy (above ≈ 25 eV), no difference is observed between the different channels. At lower kinetic energy a small difference is observable between different channels. In particular, the calculated phase difference is positive in the case of emission of an IR photon while it remains close to zero in the case of absorption of a photon. Nonetheless, the phase difference remains very small (<20 mrad) for kinetic energies down to 10 eV and it is almost the same for neon and krypton atoms. This may indicate that in the spectral region between 10 and 25 eV, the (universal) centrifugal potential starts affecting the CC phases. Below 10 eV, the difference between the channels diverges and clear differences can be observed between the different atoms, indicating the onset of atom-specific short-range effects in CC transitions.

These results are important because they show that the universality of the CC phase is not tied to the validity of the asymptotic approximation. This has also been pointed out when comparing noble gas atoms and negative ions [84]. Physically this universality can be understood in analogy to classical electrodynamics, where the interaction of a charged particle with an electrical field leads to bremsstrahlung or inverse bremsstrahlung effects. In this context, continuum–continuum transitions can be seen as stimulated one-photon bremsstrahlung. In terms of group delays the CC phase induces an additional advance (delay)[9] of the EWP for the absorption (emission) process in addition to the dynamical one-photon Wigner delay. The universality of the CC transition phases and amplitudes (through Fano's propensity rule) offers the possibility to recover information on single-photon ionization using angle-resolved interferometric two-photon measurement schemes [53].

1.2.2.4   Angle-Integrated and Angle-Resolved Measurement

Finally, we introduce a set of useful notations to discuss the angle-integrated and angle-resolved two-photon ionization measurements. For each angular-momentum path, we define

$$a_{L\lambda m}^{(\pm)}(\tau) = \mathcal{E}_{\mathrm{XUV}}(\Omega)\mathcal{E}_{\mathrm{IR}}(\omega)e^{\pm i\omega\tau}M_{L\lambda m}^{(\pm)}, \tag{1.14}$$

where $\mathcal{E}_{\mathrm{IR}}$ is the amplitude of the laser field and τ the delay between the XUV and laser fields. We further introduce the quantities

$$\mathcal{A}_{L\lambda m}^{(\pm)}(\theta, \phi, \tau) = a_{L\lambda m}^{(\pm)}(\tau)Y_{Lm}(\theta, \phi), \tag{1.15}$$

$$A_{L\lambda m}^{(\pm)}(\theta, \tau) = (-1)^m a_{L\lambda m}^{(\pm)}(\tau)\sqrt{\frac{(2L+1)(L-m)!}{2(L+m)!}}P_L^m(\cos\theta), \tag{1.16}$$

where P_L^m are the associated Legendre polynomials related to the spherical harmonics by

$$Y_{Lm}(\theta, \phi) = (-1)^m\sqrt{\frac{(2L+1)(L-m)!}{4\pi(L+m)!}}P_L^m(\cos\theta)e^{im\phi}. \tag{1.17}$$

The total angle-resolved signal is given by the modulus square of the sum over the transition amplitudes to all accessible final states. When the ionic state is not measured, the ionization probabilities corresponding to different final m states add incoherently,

---

[9] This delay is defined as the *derivative* of the CC phase with energy and should not be confused with the τ delay, which depends on the *difference* between the emission and absorption CC phases, see Sect. 1.3.

$$S^{(\pm)}(\theta, \phi, \tau) = \sum_m \left| \sum_{L,\lambda} \mathcal{A}^{(\pm)}_{L\lambda m}(\theta, \phi, \tau) \right|^2. \qquad (1.18)$$

If the photoelectron signal is integrated over all azimuthal angles, the former expression reduces to

$$\mathcal{S}^{(\pm)}(\theta, \tau) = \int_0^{2\pi} S^{(\pm)}(\theta, \phi, \tau) d\phi = \sum_m \left| \sum_{L,\lambda} A^{(\pm)}_{L\lambda m}(\theta, \tau) \right|^2. \qquad (1.19)$$

Finally, due to the orthogonality of the spherical harmonics, and of the Legendre Polynomials, the total angle-integrated signal, $S^{(\pm)}$, corresponds to the incoherent sum of the transition amplitudes to all final states

$$S^{(\pm)}(\tau) = \int_0^{\pi} \mathcal{S}^{(\pm)}(\theta, \tau) \sin\theta d\theta = \sum_{L,m} \left| \sum_{\lambda} a^{(\pm)}_{L\lambda m}(\tau) \right|^2, \qquad (1.20)$$

where only intermediate angular momentum paths that lead to the same final state are added coherently. Even for a single final state, when λ can take two values, the total phase of the two-photon transition amplitude does not correspond to that of the individual channels.

1.3 Measuring Photoionization Time Delays with RABBIT

High-order harmonic generation in gases produces a coherent comb of odd harmonics which is used to photoionize an atom. The resulting photoelectron spectrum (PES) exhibits a series of peaks due to the comb structure for the XUV. When the XUV and IR laser fields are overlapped, additional peaks, called sidebands, appear in the PES due to absorption or emission of an IR photon between continuum states. Because two consecutive harmonics are spaced by the equivalent of two IR photons, a given sideband can be reached via two quantum paths as shown in Fig. 1.5(a): absorption of one harmonic plus absorption of one IR photon or absorption of the following harmonic plus emission of one IR photon. As a result, the signal of sideband q, which corresponds to a net absorption of energy equal to $q\hbar\omega$, is given by

$$\begin{aligned} S_q &= \left| \mathcal{A}^{(+)}_{q-1} + \mathcal{A}^{(-)}_{q+1} \right|^2 \\ &= \left| \mathcal{A}^{(+)}_{q-1} \right|^2 + \left| \mathcal{A}^{(-)}_{q+1} \right|^2 + 2 \left| \mathcal{A}^{(+)}_{q-1} \right| \left| \mathcal{A}^{(-)}_{q+1} \right| \cos(2\omega\tau - \Delta\varphi), \end{aligned} \qquad (1.21)$$

where $\mathcal{A}^{(\pm)}_{q\mp 1}$ is the two-photon transition amplitude corresponding to absorption of harmonic $q \mp 1$ and absorption $(+)$ or emission $(-)$ of an IR photon. This quantity
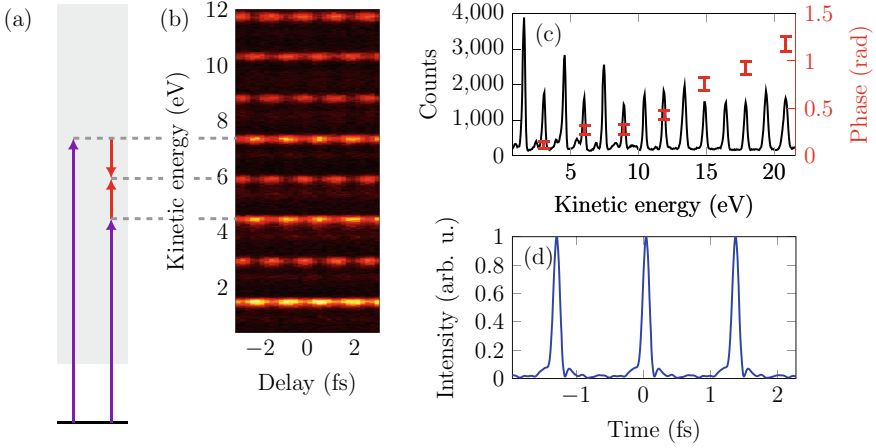
Fig. 1.5 Characterization of an attosecond pulse train. **a** Schematic representation of the RABBIT technique. **b** Low energy part of a RABBIT scan in Ne from harmonics generated in Ne. **c** Delay integrated photoelectron spectrum and phase measured at the sidebands. **d** Reconstructed attosecond pulse train. Figures taken from [77]

is angle- and channel-dependent as we will discuss in the next sections. Here, we use a compact notation to illustrate the principle of the RABBIT technique. $\mathcal{A}_{q\mp1}^{(\pm)}$ can be expressed as

$$\mathcal{A}_{q\mp1}^{(\pm)} = \mathcal{E}_{q\mp1}(\Omega_{q\mp1})\mathcal{E}_{\text{IR}}(\omega)e^{\pm i\omega\tau}M_{\mathbf{k}g}^{(\pm)}(\Omega_{q\mp1}), \qquad (1.22)$$

where $\Omega_{q\mp1} = (q \mp 1)\omega$ and $\mathcal{E}_{q\mp1}$ is the complex amplitude of the $q \mp 1$ harmonic field. The interference of the two paths to the sideband gives rise to oscillations of the sideband intensity as a function of the delay τ between the XUV and IR fields as shown in Fig. 1.5(b). The phase of these oscillations, $\Delta\varphi$, can be decomposed into two contributions, $\Delta\varphi = \Delta\varphi_{\text{XUV}} + \Delta\varphi_{\text{A}}$ which are defined as [22]:

$$\begin{aligned}
\Delta\varphi_{\text{XUV}} &= \arg\left[\mathcal{E}_{q+1}(\Omega_{q+1})\right] - \arg\left[\mathcal{E}_{q-1}(\Omega_{q-1})\right] \\
\Delta\varphi_{\text{A}} &= \arg\left[M_{\mathbf{k}g}^{(-)}(\Omega_{q+1})\right] - \arg\left[M_{\mathbf{k}g}^{(+)}(\Omega_{q-1})\right].
\end{aligned} \qquad (1.23)$$

$\Delta\varphi_{\text{XUV}}$ originates from the fact that the attosecond pulses produced by HHG are intrinsically chirped such that consecutive harmonics have different spectral phases. Usually, this phase difference varies linearly as a function of the sideband order. This effect is called 'attochirp'. $\Delta\varphi_{\text{A}}$ is the phase difference between the two-photon transition matrix elements, called the atomic phase. By fitting the sideband oscillation with Eq. (1.21), the phase offset for the different sidebands can be extracted as shown in Fig. 1.5(c). The measured phase can be related to a time delay using a finite difference approximation of the energy derivative